2-2015

Assessing Predictive Ability of Three Auroral Precipitation Models using DMSP Energy Flux

Cory T. Lane

Ariel O. Acebal
Air Force Institute of Technology

Yihua Zheng

Recommended Citation

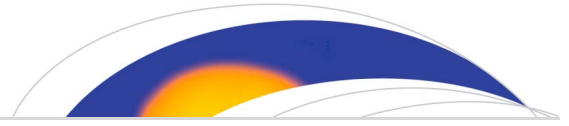Lane, C., Acebal, A. O., & Zheng, Y. (2015). Assessing predictive ability of three auroral precipitation models using DMSP energy flux. Space Weather, 13(1), 61–71. https://doi.org/10.1002/2014SW001085

Assessing predictive ability of three auroral precipitation models using DMSP energy flux

Cory Lane[1], Ariel Acebal[1], and Yihua Zheng[2]

[1]Department of Applied Physics, Air Force Institute of Technology, Wright-Patterson Air Force Base, Ohio, USA, [2]Space Weather Laboratory, NASA Goddard Space Flight Center, Greenbelt, Maryland, USA

Abstract Our study statistically compares the total energy flux outputs of Newell et al.'s (2010a) oval variation, assessment, tracking, intensity, and online nowcasting (OVATION) Prime model, Hardy et al.'s (1991) Kp-based model, and a coupled Space Weather Modeling Framework ring current model to energy flux data obtained from 2198 Defense Meteorological Satellite Program (DMSP) satellite passes in the Northern Hemisphere. Our DMSP data set includes 28 days grouped into continuous 3 and 4 day periods between 2000 and 2008 and encompasses magnetic local times (MLTs) between 04:00 and 21:00. We obtain the most equatorward magnetic latitude coordinate, where a DMSP satellite energy flux measurement exceeds 0.4 erg/cm^2/s, and use this point as a proxy for the equatorward boundary of the auroral oval in a particular MLT sector. We then calculate a prediction efficiency (PE) score by comparing the DMSP boundary coordinates to each model, using the same energy flux threshold to obtain a model's boundary location. We find that the PE for the OVATION Prime model is 0.55, and the PE for the Hardy Kp model is 0.51. When we accomplish the same analysis using a higher energy flux threshold equal to 0.6 erg/cm^2/s, the OVATION Prime model's PE increases to 0.58, while the Hardy Kp model's score drops to 0.41. Our results indicate that more complex modeling techniques, like those used in OVATION Prime, can more accurately model the auroral oval's equatorward boundary. However, Hardy's discretized Kp model, despite its relative simplicity, is still a competitive and viable modeling option.

1. Introduction

Auroral precipitation models provide one way to model space weather and are typically well suited to forecast high-latitude GPS and other communication satellite disruptions [*Griffin et al.*, 2012]. The auroral oval is commonly modeled because the characteristics of precipitating particles associated with the auroral oval can be easily observed and measured. As a result, studies of the statistical systematics of high-latitude auroral particle precipitation have proved very useful to the space weather community [*Newell et al.*, 2002; *Hardy et al.*, 2008; *Griffin et al.*, 2012].

At present, a wide variety of auroral models have been fielded, with new research aimed at validating model performance also becoming more prevalent. This defines the aim of this study in which we assess the following auroral precipitation models: (1) the oval variation, assessment, tracking, intensity, and online nowcasting (OVATION) Prime model, developed by *Newell et al.* [2002, 2010b]; (2) the *Hardy et al.*'s [1991] Kp model; and (3) a physics-based model developed by coupling data from the Space Weather Modeling Framework (SWMF) developed at the University of Michigan to a ring current model developed and maintained at the Community Coordinated Modeling Center (CCMC) at NASA Goddard.

In our study, the equatorward boundary of the auroral oval is used as the testing parameter. The equatorward auroral boundary is associated with the convection boundary formed between the zero-energy population of the plasmasphere and the lowest-energy particles in the plasma sheet. Both positively and negatively charged particles located in the Earth's magnetotail drift earthward due to crossed electric and magnetic fields. Auroral precipitation is dependent upon drifting particles in the plasma sheet and magnetotail entering the loss cone by various scattering processes. The location at which the charged particle enters the loss cone dictates the latitude where it may subsequently precipitate. During increased geomagnetic activity (i.e., high Kp), the convective electric field in the magnetotail enhances, and the charged particles
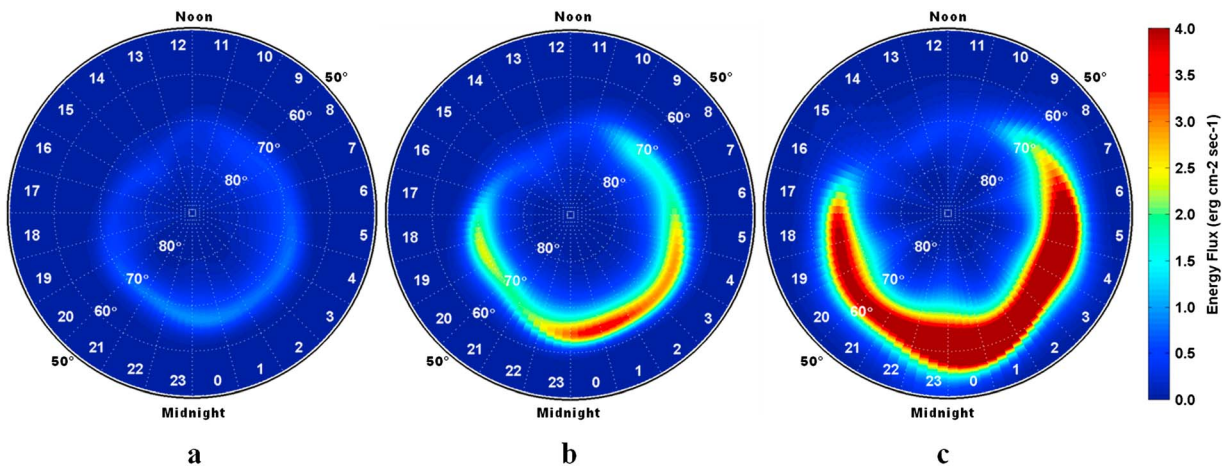
Figure 1. Polar grid plots (MLAT and MLT) of the energy flux output of the OH model for (a) $Kp = 1$, (b) $Kp = 3$, and (c) $Kp \geq 6$.

experience a correspondingly larger earthward drift [*Thomsen*, 2004]. This allows them to access magnetic field lines closer to the Earth, and they precipitate at more equatorward latitudes.

Previous studies have shown that there are several ways to define this boundary [*Gussenhoven et al.*, 1981; *Newell et al.*, 1996; *Redmon et al.*, 2010; *Griffin et al.*, 2012; *Machol et al.*, 2012]. By inspecting our Defense Meteorological Satellite Program (DMSP) data, we determined that using 0.4 erg/cm^2/s as an energy flux threshold was suitable to serve as a proxy for the equatorward boundary from which a magnetic latitude (MLAT) coordinate could be readily obtained. Because our study focuses on making point-to-point coordinate comparisons, defining the boundary using a fixed flux was appropriate despite its simplicity. We also test the models using a 0.6 erg/cm^2/s threshold as a proxy. The method we employed compared the boundary coordinate created by a model in a magnetic local time (MLT) sector to the boundary coordinate obtained from DMSP satellite data. Our assessment of each model's performance during low-, medium-, and high-Kp conditions is based upon the prediction efficiency scores.

2. Auroral Precipitation Models

2.1. Original Hardy Model

Data obtained between 1977 and 1980 from more than 27,000 orbits of three DMSP satellites were utilized in 1985 to create the Hardy Kp model [*Hardy et al.*, 1985], which was later modified to include ion precipitation [*Hardy et al.*, 1991]. Hereafter, for simplicity, we will refer to this as the original Hardy (OH) model. The OH model depicts the global pattern of electron and ion precipitation in the high-latitude region as a function of MLT, MLAT, and Kp. This model calculates energy flux values in each of 1440 MLT-MLAT high-latitude grid elements. The model's grid contains 48 MLT bins and 30 MLAT bins spanning 50°–90°. We used a simple interpolating function to increase the number of MLT bins to 240. The OH model outputs seven discrete energy flux plots for each integer value of Kp from 0 to 5 and an additional plot for all conditions of $Kp = 6$ or greater. Additional information on this model can be found in *Hardy et al.* [1985, 1991]. In Figure 1, we provide polar grid plots of energy flux for $Kp = 1$, $Kp = 3$, and $Kp \geq 6$ using 240 MLT bins.

2.2. The OVATION Prime Model

The OVATION Prime (OP) model [*Newell et al.*, 2010a] can be used to compute energy flux; however, its output is not discretely parameterized by Kp index. Instead, the OP model is parameterized by solar wind driving, represented by the following solar wind coupling function [*Newell et al.*, 2007]:

$$\frac{d\phi_{MP}}{dt} = v^{4/3} \cdot B^{2/3} \cdot \sin^{8/3}\left(\frac{\theta}{2}\right)$$

where $d\phi_{MP}/dt$ is the magnetic flux at the magnetopause, v is the bulk solar wind velocity (km/s), B is the $\left(B_y^2 + B_z^2\right)^{1/2}$ (nT), and θ is the interplanetary magnetic field clock angle. The solar wind data for historical runs of this model come from the OMNI2 data supplied by NASA Goddard.
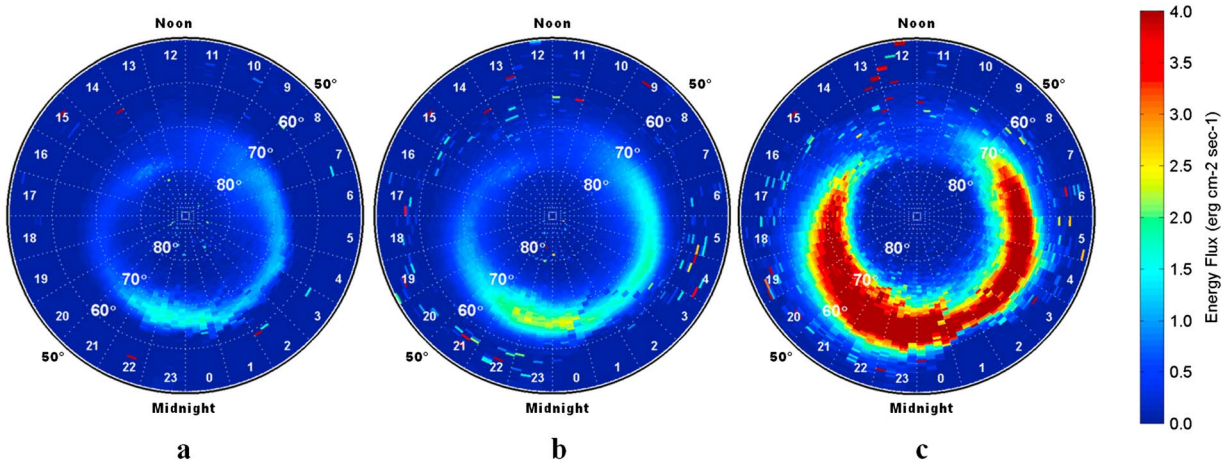
Figure 2. Polar grid plots (MLAT and MLT) of the energy flux output of the OP model during (a) $Kp = 1$, (b) $Kp = 3$, and (c) $Kp = 6$ conditions.

This solar wind coupling function serves as an organizing parameter for the model, and the statistical analysis is based upon the least squares regression of the form

$$\text{Auroral Power}\left(\frac{d\phi_{MP}}{dt}\right) = a + b \cdot \frac{d\phi_{MP}}{dt}$$

where the auroral power is calculated in each grid element. There are 46,080 individual regression fits which constitute the model (4 categories × 120 MLAT bins × 96 MLT bins). The model then calculates the energy flux in a specific MLT-MLAT bin by taking the product of the fitted estimate of the auroral intensity and the probability of observing the specific type of aurora. OP possesses the capability to model electron and ion aurora independently [*Newell et al.*, 2010b]. In our study, we did not investigate this feature of the OP model and instead used the total energy flux defined as the sum of the fluxes of all contributing particles. In 2013, Newell et al. fielded a new version of OP. We did not test this particular version, although we feel that our results still provide a valuable characterization of the OP model's unique method. The representative polar grid plots of the 2010 version of the OP model are shown in Figure 2. These model runs were accomplished at arbitrarily chosen times when the *Kp* index was $Kp = 1$, $Kp = 3$, and $Kp = 6$ and thus represent three specific model outputs.

2.3. Space Weather Modeling Framework Model

The Space Weather Modeling Framework (SWMF), developed at the University of Michigan, consists of 10 major components covering the entire domain of solar-terrestrial space weather (http://csem.engin. umich.edu/SWMF/). It is hosted and maintained at the Community Coordinated Modeling Center (CCMC; http://ccmc.gsfc.nasa.gov). A method to calculate auroral precipitation patterns requires coupling the global magnetosphere (GM) component of the SWMF, the Block-Adaptive-Tree-Solarwind-Roe-Upwind-Scheme, to the Fok ring current (RC) model [*Fok et al.*, 2001].

In this process, the SWMF/GM model provides a physics-based magnetohydrodynamic characterization of the Earth's magnetosphere [*Tóth et al.*, 2005]. The Fok RC model is then used to generate a kinetic description of the global particle distribution in the inner magnetosphere in the energy range of 1–300 keV. By taking advantage of the dynamic electric and magnetic fields modeled by SWMF/GM, the Fok RC model computes the equatorward boundary of auroral precipitation patterns.

For simplicity, this model will be referred to as the SWMF-RC model. The current SWMF-RC model assumes that 30% of the particle fluxes crossing the equatorial plane in the magnetosphere are scattered into the loss cone, where they precipitate into the ionosphere. A better calculation of precipitation will be explored in the future. The model provides precipitating energy flux and characteristic energy (average energy) at the ionosphere. The most equatorward location is determined in the same fashion as other models by applying a specified energy flux threshold. The resolution of the SWMF-RC model is 1 h MLT, meaning, it only calculated 24 boundary locations. At this time, it is not possible to create an entire polar grid plot for the SWMF model.
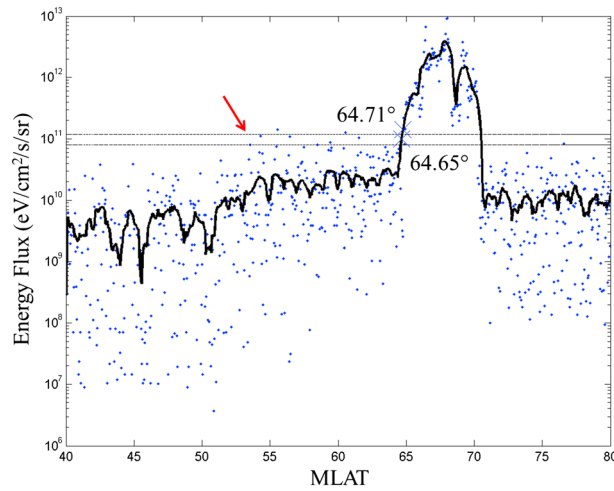
Figure 3. Data taken from DMSP satellite F15 on 31 August 2001 during low-*Kp* conditions. Energy flux thresholds are 8.0×10^{10} and 1.2×10^{11} eV/cm^2/s/sr. The diagonal arrow points to false boundary. The *X* symbols designate the location of the equatorward boundary found at 64.65° and 64.71° MLAT, respectively.

3. Methodology

3.1. DMSP Boundaries

Energy flux data are recorded at 1 s intervalsby the Special Sensor Precipitating Electron and Ion Spectrometer (SSJ/4 or SSJ/5) installed on each DMSP satellite. These data were processed to determine the MLAT and MLT coordinates of the equatorward boundary of the auroral oval using our predefined energy flux thresholds. In Figure 3, the total ion and electron energy flux data obtained during a northbound pass of DMSP satellite F15 on 31 August 2001 are plotted as a function of MLAT. At the time the boundary was crossed, the satellite was flying on the Earth's nightside. As other studies have shown [e.g., *Gussenhoven et al.*, 1981], the rapid energy onset at the boundary location evident in this example is a somewhat

dependable characteristic of the nightside auroral boundary. The horizontal dashed lines show our 0.4 erg/cm^2/s and 0.6 erg/cm^2/s energy flux thresholds, for which boundary crossing coordinates of 64.65° and 64.71° MLAT, respectively, were recorded. Both of the flux thresholds are clearly above the average energy measurements made on the equatorward side of the auroral oval. It was through inspection of the remainder of our DMSP data that we determined our flux thresholds, albeit arbitrary, were accurate proxies for the equatorward boundary. However, to account for the directional dependence of the DMSP sensor data, we converted these thresholds to 8.0×10^{10} eV/cm^2/s/sr and 1.2×10^{10} eV/cm^2/s/sr by dividing the flux by π.

We utilized a 15 s moving average of the individual energy flux measurements, depicted by the solid black curve in Figure 3, to identify the boundary location. Because of the typically rapid onset of energy, especially in the night sectors, we determined that using this averaging technique had no adverse effect on our subsequent analysis but was necessary to prevent recording false boundary locations like the one shown by the diagonal arrow in Figure 3.

Our study used data obtained on 28 days between 2000 and 2008 during varying geophysical conditions (Table 1). We grouped the days together to capture the initial and recovery phases during high-*Kp* events. On each day we studied, we obtained DMSP data from three different satellites to mitigate the effects of any singular satellite bias. Because of the short orbital period of the DMSP satellites, we were able to incorporate a total of 2198 DMSP boundary crossings into this study.

Table 1. List of Dates, *Kp* Range, and DMSP Satellites

Dates	*Kp* Range	DMSP Satellite No.
23/2/00–25/2/00	0.7–4.7	13, 14, and 15
31/8/01–1/9/1	0.3–4.0	14, 15, and 16
23/10/2–25/10/2	1.0–6.3	13, 14, and 15
12/10/4–14/10/4	0.7–5.0	13, 15, and 16
15/5/5–16/5/5	1.7–8.3	13, 15, and 16
9/7/5–12/7/5	2.0–6.3	13, 15, and 16
31/8/5–1/9/5	1.0–7.0	13, 15, and 16
14/12/6–16/12/6	0.7–8.3	13, 15, and 16
19/6/7–21/6/7	0.7–3.3	13, 15, and 17
26/3/8–28/3/8	1.3–5.0	15, 16, and 17

The subcategories listed in Table 2 were utilized to divide our large data set into smaller categories based on time *Kp*. This enabled us to study and compare model behavior during similar *Kp* conditions.

3.2. Determining Model Boundaries

To obtain a model boundary coordinate to compare to the corresponding DMSP coordinate, the DMSP timestamp of a threshold crossing was provided to each model as an input parameter along with

Table 2. *Kp* Subcategories

Kp	
Low	0.0–2.7
Middle	3.0–6.0
High	6.3–9.0

any additional data required (e.g., *Kp*). The DMSP MLT coordinate was rounded to match the model's resolution, and each model's output was then interrogated in that MLT sector. Then, the most equatorward coordinate (MLAT) equaling or exceeding our energy flux threshold was recorded.

The older version of the OP model we used in our study occasionally produced large fluxes at singular grid elements in the low magnetic latitudes. This anomaly is a numerical computation by-product of the high fidelity that the model offers [*Newell et al.*, 2014]. To combat this issue in the version of OP we used, we recorded an OP boundary only if three consecutive flux measurements, as measured from equatorward to poleward, met or exceeded the threshold. Using this technique increased our confidence in the OP boundary, and although it did not eliminate all of the suspicious boundary locations, there were very few instances in which these points were actually used to make a DMSP comparison. In the 2013 modification to OVATION Prime model [*Newell et al.*, 2014], this issue has been addressed and remedied, so we estimate that our results here most likely underreport the current OP model's capability.

Our access to the SWMF-RC model data was limited due to the available number of model runs at the time of our analysis. The total number of comparisons we were able to make to SWMF-RC was 426. We have included its results here because it represents a unique physics-based model.

3.3. Prediction Efficiency

This study used prediction efficiency (PE) as a means of measuring each model's accuracy. Similar studies [*Li et al.*, 2001; *Pulkkinen et al.*, 2010; *Rastätter et al.*, 2011] have successfully used PE to quantify model accuracy. Prediction efficiency describes the percentage of the variance in an observed data set that is explained by a model. PE is a numerical score with a maximum value of 1, which would indicate that 100% of the data's variance is described by the model. It has no theoretical minimum value; however, a PE ≤ 0 indicates that the model's prediction is statistically less accurate than using the mean of the observed data. Prediction efficiency is calculated using the following formula, where y_i is the DMSP MLAT coordinate and x_i is the model boundary coordinate:

$$\text{PE} = 1 - \frac{\sum_{i=1}^{N}(y_i - x_i)^2}{\sum_{i=1}^{N}(y_i - \overline{y_l})^2} \ .$$

4. Results and Analysis

Figure 4 shows six plots that depict the DMSP boundary crossings obtained between *Kp* = 1 and *Kp* = 6+ in this study projected on a MLAT-MLT polar grid. No data are present between 22:00 MLT and 03:00 MLT because of the nature of the satellite orbits. The sparse coverage obtained between approximately 13 and 15 MLT, especially at higher *Kp* levels, is also an artifact of the DMSP satellite orbit characteristics during the years covered in this study. Nevertheless, our data still adequately cover the boundary on both the sunward and antisunward sides of the Earth. In Figure 5, we summarize the distribution of our data as a function of MLT.

The boundary locations depicted in Figure 4 also qualitatively depict the systematic equatorward expansion of the boundary with increasing *Kp* value also reported in other studies [e.g., *Redmon et al.*, 2010]. What is also apparent is the substantial variance in the DMSP data, which in some cases spans more than 20° MLAT in the same MLT sector at the same *Kp*. We selected prediction efficiency as our primary statistic because it addresses the amount of variance accounted for by the models.

4.1. Quantitative Comparison Using Prediction Efficiency

The results of our prediction efficiency calculations are presented in Table 3. In addition to calculating a score using all of the data points, we also divided the results into *Kp* groups and further subdivided into MLT sectors. We indicate a negative PE score by a double dash (--), because there is no meaning to the value of a PE score less than zero. To avoid anomalies associated with small sample sets, a PE score was not determined in subgroups with fewer than 20 data points.
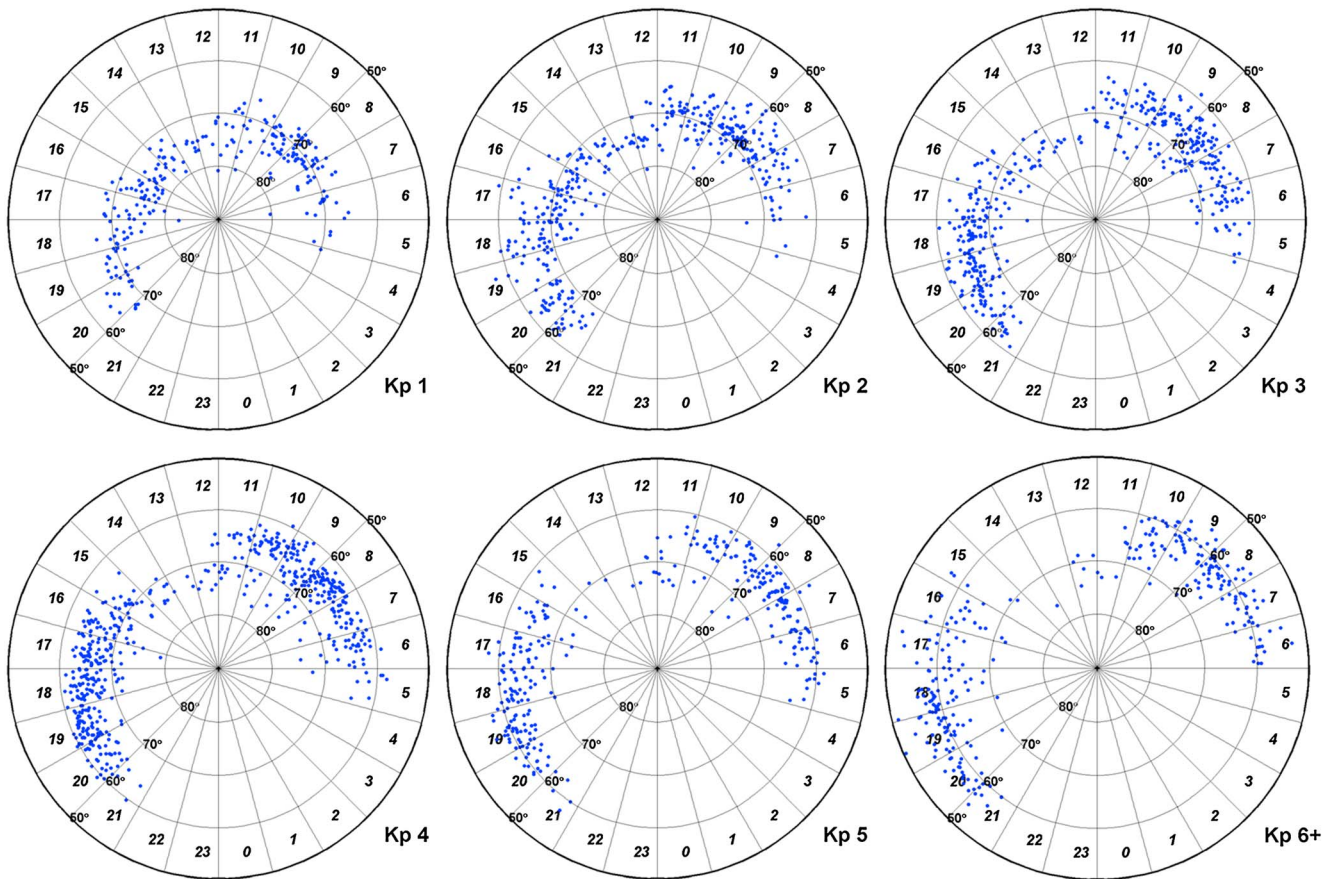
Figure 4. Polar grid plots (MLAT and MLT) showing DMSP boundary crossings in the Northern Hemisphere with an energy flux threshold of 8.0×10^{10} eV/cm^2/s/sr. Data are binned by integer value of *Kp*, where *Kp* = 6+ represents data obtained during *Kp* conditions equal to and greater than *Kp* = 6.

The top line of Table 3 lists the PE scores using the entire data set, independent of all subcategories. Here the OP model has the highest PE score, indicating that it accounts for 55% of the variance observed in the DMSP data. The OH model accounts for 51% of the variance. The size of the sample (*N*) equals 2198 (the total number of DMSP boundaries obtained) in neither cases because of situations where OH and OP failed to provide a corresponding 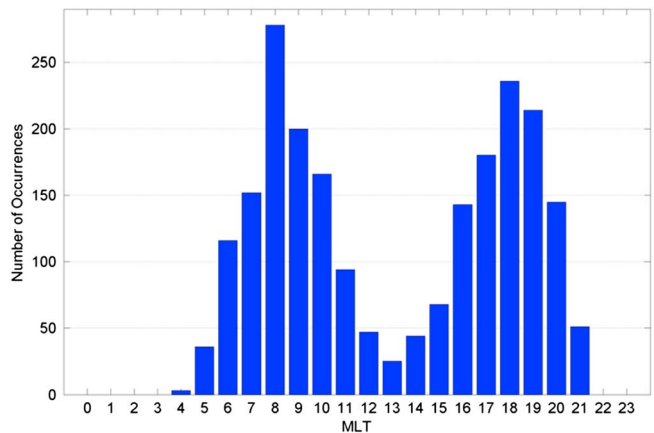boundary to a valid DMSP data point. During our analysis, we discovered that the existence of a boundary in the DMSP data did not guarantee the existence of a corresponding boundary in one or more of the models, particularly if the *Kp* was less than 2.0 and/or the boundary was located between 11 and 13 MLT. In effect, the model missed placing the boundary by failing to produce any fluxes above our threshold. If a boundary was not generated by a model, we elected to remove the data point from our study. Thus, out of the 2198 DMSP boundaries obtained, the corresponding number of crossings determined using the OH and OP models was 2059 and 2122, respectively. We depict these missed

Figure 5. Distribution of boundary data as a function of MLT. The data between 13 and 15 MLT are limited due to the Sun-synchronous orbits of the DMSP satellites.

Table 3. Prediction Efficiency Scores Using 0.4 erg/cm^2/s Threshold[a]

MLT	Kp	OH	OP	SWMF-RC
04–21	All levels	0.51 (2059)	**0.55 (2122)**	-- (426)
04–21	High	-- (140)	0.13 (140)	**0.29 (103)**
	Middle	**0.31 (1315)**	0.30 (1319)	-- (215)
	Low	0.34 (604)	**0.37 (663)**	-- (108)
04–09	High	-- (58)	-- (58)	**0.32 (43)**
	Middle	0.05 (486)	**0.30 (486)**	-- (88)
	Low	0.06 (231)	**0.10 (241)**	-- (25)
10–15	High	(15)	(15)	(10)
	Middle	**0.21 (213)**	0.12 (218)	-- (27)
	Low	**0.40 (130)**	0.38 (145)	-- (38)
16–21	High	-- (67)	0.15 (67)	**0.25 (50)**
	Middle	**0.35 (616)**	0.19 (615)	-- (100)
	Low	0.36 (243)	**0.37 (277)**	-- (45)

[a]Negative PEs are indicated by double dash (--). The numbers in parentheses indicate size of the sample (*N*) used to calculate the PE. The bold entries denote the highest PE in that category.

boundaries in Figure 6, which depict overlays of the data losses in each hourly MLT sector. At 0.4 erg/cm^2/s, the OP model losses a total 3.5%, and the OH model losses a total 6.3% of the available DMSP data. However, it is the location of these losses that underpins the increased difficulty of modeling auroral precipitation originating in the dayside magnetosphere (near 12 MLT). At the higher threshold, the number of total missing boundaries increases to 19.3% for OP and 21.6% for OH, with both models missing nearly 100% of the DMSP boundaries between 11 and 13 MLT. This indicates that increases in energy flux observed by DMSP are often missed by both models in the day MLT sectors during low-*Kp* conditions. The SWMF-RC model did not
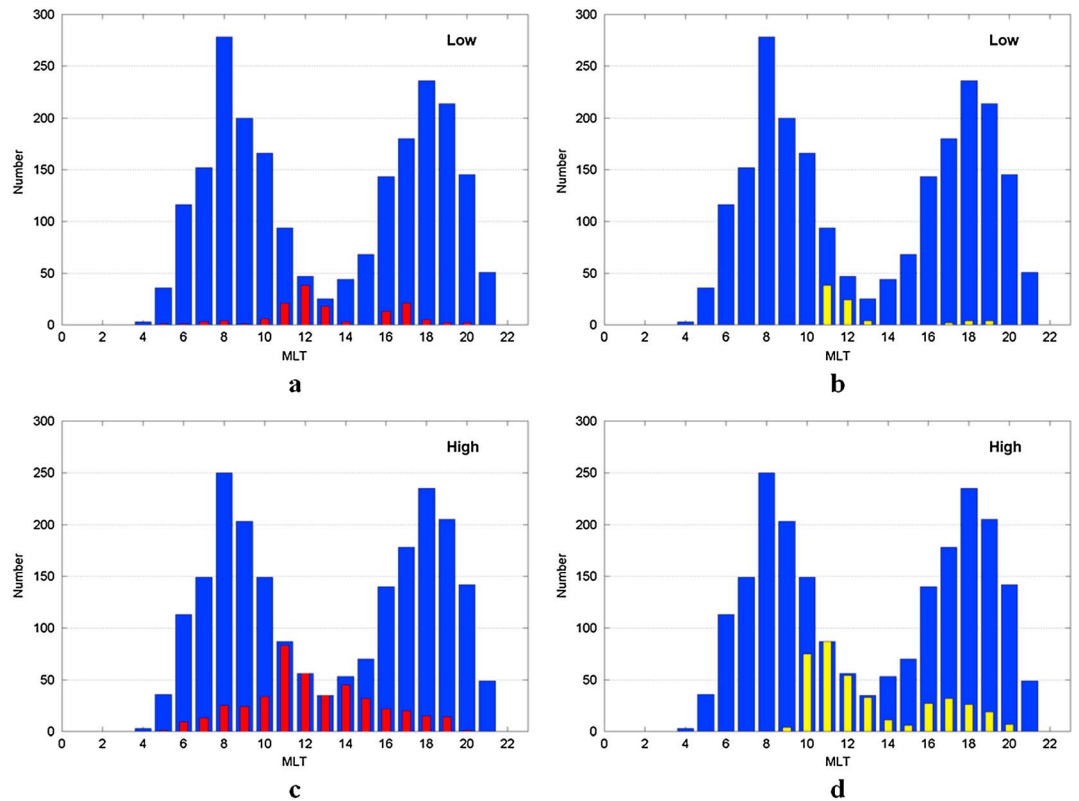

Figure 6. Distribution plot of (a) OH model and (b) OP model boundaries obtained in each MLT sector using 0.4 erg/cm^2/s ("low") threshold with the number of boundary misses overlaid. (c and d) Boundary misses using 0.6 erg/cm^2/s ("high") threshold are shown.
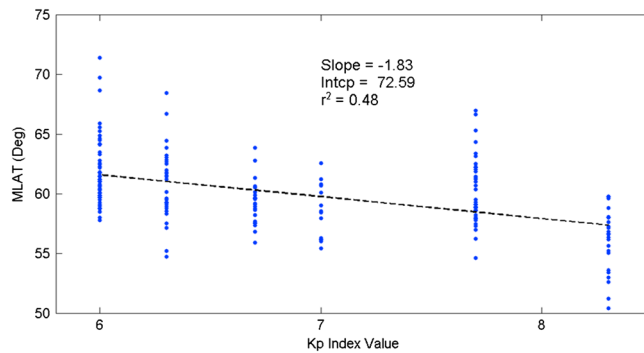
Figure 7. DMSP MLAT coordinates as a function of *Kp* showing continued migration of boundary equatorward during *Kp* conditions above *Kp* = 6.

have any misses, so no SWMF-RC data are shown. Its small sample size is solely due to the limited number of model runs available.

The SWMF's PE scores fall below zero for the majority of the subcategories. However, it has a higher PE score than the other models during high-*Kp* conditions. This supports the idea that a model may be suited to (and by extension, designed to) model a particular condition well. Along those lines, we likewise observe the OH model's difficulty modeling the

auroral oval during high-*Kp* conditions. This is somewhat surprising in light of the model's obvious expansion shown in Figure 1. The fact that the OH model is not only discretized but also remains unmodified for any conditions more extreme than *Kp* = 6 likely accounts for the negative PE scores at these high-*Kp* conditions. In Figure 7, we plot a regression line of the DMSP boundary coordinates for *Kp* = 6.0–8.3 conditions that shows the boundary moving equatorward at 1.83° MLAT per integer increase in *Kp*. This expansion rate is consistent with the findings of *Carbary* [2005] who showed similar equatorward boundary migration as a function of *Kp*. This becomes the most likely contribution to PE scores below zero in this high-*Kp* category.

As Table 3 shows, each model has the highest PE scores in several of the subcategories, although some scores are quite low. Based on these results, a single best model is not apparent. We note that the generally small gap between many of the OH and OP prediction efficiency scores, despite their vastly different approaches to modeling, may itself be significant result.

4.2. Analysis at a Higher Energy Flux Threshold

In order to eliminate any unforeseen bias that may have been present using 0.4 erg/cm^2/s, the entirety of the previous PE analysis was repeated using a 0.6 erg/cm^2/s energy flux threshold, equating to 1.2×10^{11} eV/cm^2/s/sr. As Figure 3 shows, at the higher energy flux threshold, the boundary location's poleward shift is virtually imperceptible, but model misses substantially increased at this new threshold. In Figure 8, we reproduce Figure 4 including the boundary crossing points at the higher threshold in red. The fact that no extreme poleward shift appears, especially between 18:00 and 21:00 MLT, is another indicator of the steep energy flux gradient that occurs on the nightside of the Earth.

Because our study eliminated all model misses without penalty to the models' performances, our PE scores during low-*Kp* conditions likely overestimate the models' abilities. Table 4 lists each model's difference statistics using the new threshold, where the smaller sample sizes (*N*) for the OH and OP models are again due entirely to model misses, and the SWMF-RC reduction is again due to a limited number of model runs.

Comparing the models' scores at a higher threshold permits some general conclusions. When the higher energy flux is utilized, the OP model outperforms OH and SWMF-RC in most of the categories, although it still accounts for less than 60% of the variance observed in the DMSP data. The reasons for OP's relative success at the higher threshold are not readily apparent, but these results, combined with results at the lower threshold, do validate the OP model's more complex way of modeling and utilization of a solar wind coupling function. At the higher threshold, the OH model's drop in performance is certainly noticeable but is difficult to attribute an obvious cause.

These results are similar to *Newell et al.*'s [2010b] study of various auroral models' abilities to predict hemispheric auroral power by comparison to Polar Ultraviolet Imager (UVI) images. They also studied the OP and OH models and found that the OP model accounted for 56% of the variance in Polar UVI data, with the OH model accounting for 52%. Our comments about overall model performance could echo this—namely, that the more complex models tend to improve the model's accuracy, although perhaps not as much as one might anticipate. This is particularly true in light of the differences in the basic function of the OH and OP models. The *Kp* parameter is only updated at 3 h intervals, whereas the parameters
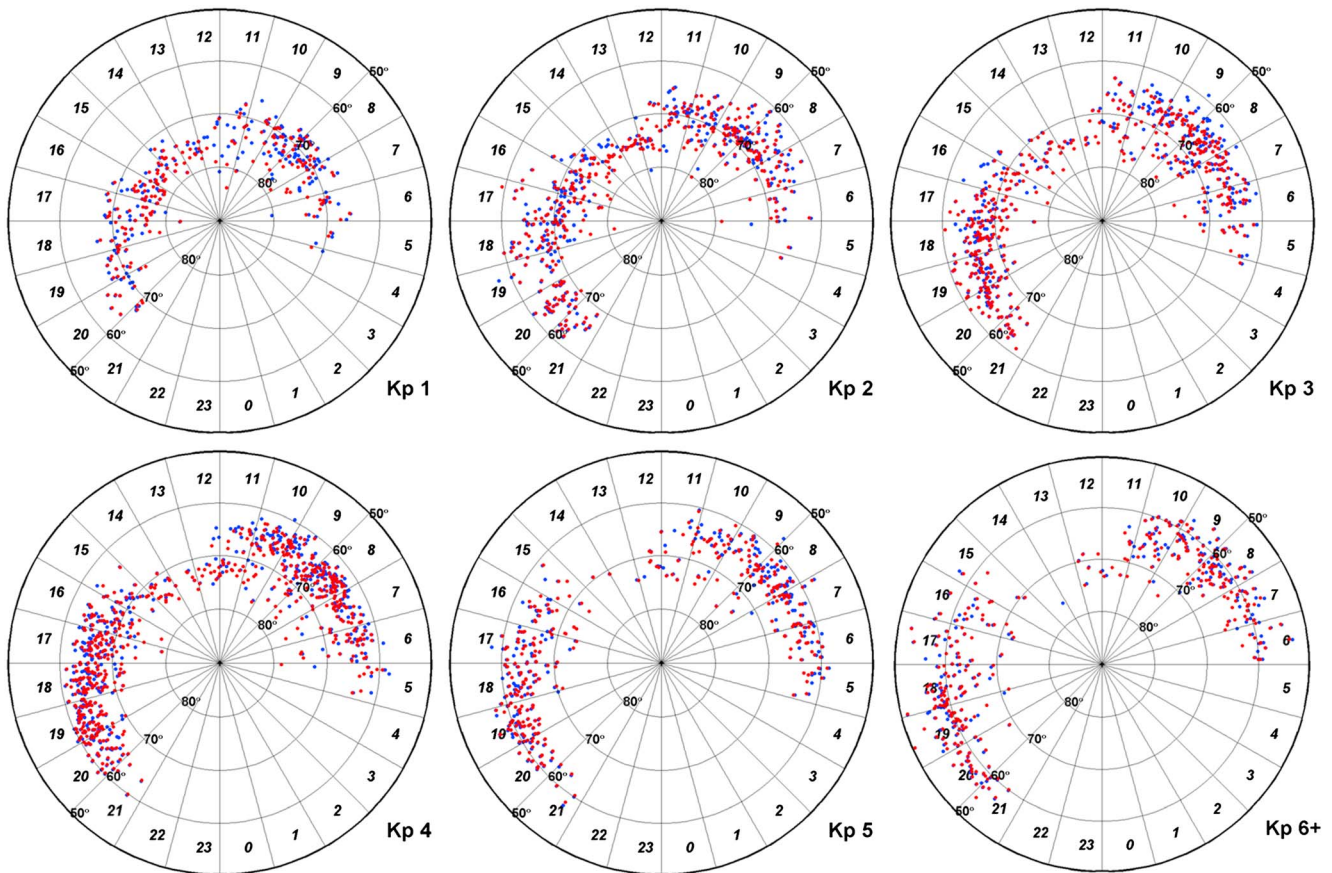
Figure 8. Same as Figure 4 with DMSP boundaries corresponding to an energy flux threshold of 8.0×10^{10} eV/cm^2/s/sr (blue) and 1.2×10^{11} eV/cm^2/s/sr (red).

in the OP model's coupling function are updated every minute. From this perspective, the OH model's prediction efficiency scores are surprisingly close to OP's.

We also acknowledge that the relatively low prediction efficiency scores do not necessarily characterize model shortcomings. The selection of fixed energy flux thresholds as a testing parameter was made objectively but somewhat arbitrarily. Selection of additional testing parameters may discover other boundary types for which the models' prediction capabilities increase or which take advantage of the faster refresh capability.

Table 4. Prediction Efficiency Scores Using 0.6 erg/cm^2/s Threshold[a]

MLT	Kp	OH	OP	SWMF-RC
04–21	All levels	0.41 (1724)	**0.58 (1772)**	-- (320)
04–21	High	-- (128)	0.16 (139)	**0.24 (31)**
	Middle	0.29 (1201)	**0.39 (1177)**	-- (208)
	Low	0.11 (395)	**0.47 (456)**	-- (81)
04–09	High	-- (55)	-- (55)	(9)
	Middle	0.17 (479)	**0.31 (479)**	-- (72)
	Low	-- (148)	**0.20 (216)**	-- (25)
10–15	High	(5)	(16)	(5)
	Middle	0.12 (101)	**0.40 (110)**	-- (41)
	Low	0.17 (59)	**0.58 (58)**	-- (18)
16–21	High	-- (68)	**0.29 (68)**	0.16 (17)
	Middle	**0.40 (621)**	0.32 (588)	-- (95)
	Low	0.13 (188)	**0.40 (182)**	-- (38)

[a]Negative PEs are indicated by a double dash (--). The numbers in parentheses indicate size of the sample (N) used to calculate the PE. The bold entries denote the highest PE in that category.

5. Summary

This study quantitatively assessed the accuracy of three auroral precipitation models by comparing them to DMSP measurements. Data from more than 2000 DMSP satellite passes obtained over 28 days between 2000 and 2008 were included. It was determined that despite a high degree of variance, the location of the equatorward boundary could be determined using the DMSP data by selecting a fixed energy flux as a proxy. We measured the accuracy by comparing each model's location of a specific energy flux to the DMSP satellite data and calculated a prediction efficiency score.

The models studied here highlighted different approaches to modeling, and the characteristic behavior of each model was investigated under a variety of geomagnetic conditions. The prediction efficiency of each model was calculated using a 0.4 erg/cm^2/s threshold and a 0.6 erg/cm^2/s threshold. The first set of PE scores led to the general conclusion that the OP model exhibited the highest degree of accuracy, and the SWMF model proved to be effective at modeling the aurora during most high-*Kp* conditions. The PE scores calculated for the data obtained with the 0.6 erg/cm^2/s threshold showed an uptick in the performance of the OP model, affirming its place as the top performer.

The results of this study are consistent with our understanding of the limitations of empirical models (OH), semiempirical models (OP), and physical models (SWMF-RC). Empirical models adequately and accurately capture the general trends of auroral oval expansion but tend to lose smaller-scale fidelity. Finely tuned semiempirical models attempt to replicate some of these small-scale features with an increase in the ability to predict the sharp energy flux boundaries. Physical models show promise, especially as computational efficiencies continue to increase, but there are very sensitive constraints placed upon input parameters.

The OVATION Prime model's overall prediction efficiency scores at 0.4 erg/cm^2/s and 0.6 erg/cm^2/s were 0.55 and 0.58, respectively. The Hardy *Kp* model's scores were 0.51 and 0.41. Our analysis of these models at least partially underscores the significant challenges auroral modeling efforts face. However, it is also clear that these efforts are heading in the right direction and converging on substantial improvements, which will certainly be of great benefit as reliance upon space-based assets continues to grow.

References

Carbary, J. F. (2005), A Kp-based model of auroral boundaries, *Space Weather*, *3*, S10001, doi:10.1029/2005SW000162.
Fok, M.-C., R. A. Wolf, R. W. Spiro, and T. E. Moore (2001), Comprehensive computational model of the Earth's ring current, *J. Geophys. Res.*, *106*(A5), 8417–8424, doi:10.1029/2000JA000235.
Griffin, J. M., T. C. Connor, and H. E. Snell (2012), Use of the auroral boundary index for potential forecasting of ionospheric scintillation, *Radio Sci.*, *47*, RS0L19, doi:10.1029/2011RS004954.
Gussenhoven, M. S., D. A. Hardy, and W. J. Burke (1981), DMSP/F2 electron observations of equatorward auroral boundaries and their relationship to magnetospheric electric fields, *J. Geophys. Res.*, *86*(A2), 768–778, doi:10.1029/JA086iA02p00768.
Hardy, D. A., M. S. Gussenhoven, and E. Holeman (1985), A statistical model of auroral electron precipitation, *J. Geophys. Res.*, *90*(A5), 4229–4248, doi:10.1029/JA090iA05p04229.
Hardy, D. A., W. McNeil, M. S. Gussenhoven, and D. Brautigam (1991), A statistical model of auroral ion precipitation: 2 functional representation of the average patterns, *J. Geophys. Res.*, *96*(A4), 5539–5547, doi:10.1029/90JA02451.
Hardy, D. A., E. G. Holeman, W. J. Burke, L. C. Gentile, and K. H. Bounar (2008), Probability distributions of electron precipitation at high magnetic latitudes, *J. Geophys. Res.*, *113*(A6), doi:10.1029/2007JA012746.
Li, X., M. Temerin, D. N. Baker, G. D. Reeves, and D. Larson (2001), Quantitative prediction of radiation belt electrons at geostationary orbit based on solar wind measurements, *Geophys. Res. Lett.*, *28*(9), 1887–1890, doi:10.1029/2000GL012681.
Machol, J. L., J. C. Green, R. J. Redmon, R. A. Viereck, and P. T. Newell (2012), Evaluation of OVATION Prime as a forecast model for visible aurorae, *Space Weather*, *10*, S03005, doi:10.1029/2011SW000746.
Newell, P., Y. Feldstein, Y. Galperin, and C.-I. Meng (1996), Morphology of nightside precipitation, *J. Geophys. Res.*, *101*(A5), 10,737–10,748, doi:10.1029/95JA03516.
Newell, P. T., T. Sotirelis, J. M. Ruohoniemi, J. F. Carbary, K. Liou, J. P. Skura, C.-I. Meng, C. Deehr, D. Wilkinson, and F. J. Rich (2002), OVATION: Oval variation assessment, tracking, intensity, and online nowcasting, *Ann. Geophys.*, *20*, 1039–1047.
Newell, P. T., T. Sotirelis, K. Liou, C. I. Meng, and F. J. Rich (2007), A nearly universal solar wind-magnetosphere coupling function inferred from 10 magnetospheric state variables, *J. Geophys. Res.*, *112*, doi:10.1029/2006JA012015.
Newell, P. T., T. Sotirelis, and S. Wing (2010a), Seasonal variations in diffuse, monoenergetic, and broadband aurora, *J. Geophys. Res.*, *115*, doi:10.1029/2009JA014805.
Newell, P. T., T. Sotirelis, K. Liou, A. R. Lee, S. Wing, J. Green, and R. Redmon (2010b), Predictive ability of four auroral precipitation models as evaluated using Polar UVI global images, *Space Weather*, *8*, S12004, doi:10.1029/2010SW000604.
Newell, P. T., K. Liou, Y. Zhang, T. Sotirelis, L. J. Paxton, and E. J. Mitchell (2014), OVATION Prime-2013: Extension of auroral precipitation model to higher disturbance levels, *Space Weather*, *12*, 368–379, doi:10.1002/2014SW001056.
Pulkkinen, A., L. Rastätter, M. Kuznetsova, M. Hesse, A. Ridley, J. Raeder, H. J. Singer, and A. Chulaki (2010), Systematic evaluation of ground and geostationary magnetic field predictions generated by global magnetohydrodynamic models, *J. Geophys. Res.*, *115*, A03206, doi:10.1029/2009JA014537.

Rastätter, L., M. M. Kuznetsova, A. Vapirev, A. Ridley, M. Wiltberger, A. Pulkkinen, M. Hesse, and H. J. Singer (2011), Geospace Environment Modeling 2008–2009 Challenge: Geosynchronous magnetic field, *Space Weather*, *9*, S04005, doi:10.1029/2010SW000617.

Redmon, R. J., W. K. Peterson, L. Andersson, E. A. Kihn, W. F. Denig, M. Hairston, and R. Coley (2010), Vertical thermal O^+ flows at 850 km in dynamic auroral boundary coordinates, *J. Geophys. Res.*, *115*, A00J08, doi:10.1029/2010JA015589.

Thomsen, M. F. (2004), Why Kp is such a good measure of magnetospheric convection, *Space Weather*, *2*, S11004, doi:10.1029/2004SW000089.

Tóth, G., et al. (2005), space weather modeling framework: A new tool for the space science community, *J. Geophys. Res.*, *110*, doi:10.1029/2005JA011126.